Development of multicomponent lattice Boltzmann flux solver for simulation of compressible viscous reacting flows

Tianpeng Yang,[1] Jiangfeng Wang,[1,*] Liming Yang,[2] and Chang Shu[2]

[1]*College of Aerospace Engineering, Nanjing University of Aeronautics and Astronautics, 29 Yudao Street, Nanjing 210016, China*

[2]*Department of Mechanical Engineering, National University of Singapore, 10 Kent Ridge Crescent, Singapore 119260, Singapore*

(Received 4 May 2019; published 24 September 2019)

In this paper, the multicomponent lattice Boltzmann flux solver (LBFS) is developed for simulation of two-dimensional compressible viscous reacting flows. This work is based on the existing LBFS for simulation of single-component compressible flows. The present solver applies the finite volume method to discretize the multicomponent Navier-Stokes equations and evaluates the numerical flux at the cell interface by local solution of the lattice Boltzmann equation. To evaluate numerical flux, the original non-free parameter D1Q4 model in the existing LBFS is extended to the multicomponent counterpart in which the total density at the cell interface is computed directly by summing the density distribution functions, and the densities of different species are calculated from the mass fractions at the left and right sides of cell interface. The internal energy is evaluated from the enthalpy which considers the different physical properties of the species, and the temperature at the cell interface is obtained by Newton iteration. In addition, an improved switch function which takes into account the reacting effects and aspect ratio of the grid is introduced to control the numerical dissipation. Several benchmark problems are simulated to validate the present multicomponent LBFS. It is shown that the present solver is carbuncle-free for the unfavorable aspect ratio grid in the test cases here and has a satisfied performance for simulation of multicomponent compressible viscous reacting flows.

DOI: 10.1103/PhysRevE.100.033315

I. INTRODUCTION

As an alternative approach to simulate fluid flows, the lattice Boltzmann method (LBM) has received much attention in recent years. The standard LBM has many advantages as it is much simpler to implement than conventional methods [1], and it is appropriate for simulating mesoscopic physics phenomena, which are hard to describe macroscopically [2]. LBM has achieved great success in the simulation of various flows, such as multiphase flow [3], porous media flow [4], suspended particle flow [5], and rarefied flow [6]. However, there are few applications of LBM for the reacting flow, which involves chemical reactions, turbulent mixing, heat transfer, radiation, and many other fluid phenomena. This limitation is mainly due to the lack of proper multicomponent lattice Boltzmann (LB) models for compressible reacting flows.

In the field of LBM, there are two major kinds of multicomponent LB models. One considers the density as a constant in combustion flow. Succi *et al.* [7] first simulated the methane-air laminar flame under the hypothesis of a cold flame. In their work, two passive scalars were used to describe temperature and the fraction of the fuel in the mixture. Subsequently, Yamamoto *et al.* [8] developed a new combustion LB model by using two disconnected distribution functions to describe the density field and the temperature field, respectively. Since the density is considered as a constant, this kind of multicomponent LB model may cause a deviation from the real physical phenomenon, and the thermal flow simulations may not accurate [1]. Another kind of multicomponent LB model considers the temperature and density fields simultaneously, which can be viewed as the coupled multicomponent LB model. Filippova and Hanel [9] developed a coupled multicomponent LB model by the low-Mach-number approximation and solved the temperature field by the finite difference scheme. The disadvantage of this model is its limited temperature range, which does not satisfy the requirement of real combustion. Yan *et al.* [10] developed a coupled multicomponent LB model for simulation of the detonation process based on the assumption of a compressible fluid. In this model, the chemical reaction process and fluid dynamics process are coupled into one distribution function. It is noted that the coupled multicomponent LB model is difficult to use for describing the complex chemical kinetic model. As described above, to establish a multicomponent LB model that conforms to real physical processes and fits for a wide range of Mach number, consideration of the compressibility effect is essential. Aiming at the isothermal compressible flow, Alexander *et al.* [11] proposed a compressible LB model with adjustable sound speed to simulate fluid flows with different Mach numbers. Qu *et al.* [12] replaced the Maxwellian distribution function with a circular function and developed several one- and two-dimensional compressible LB models. However, in their models, the lattice velocities are kept

*Corresponding author: wangjf@nuaa.edu.cn

constant, which are determined by the initial Mach number and internal energy. Yang *et al.* [13] recently developed a platform for the derivation of non-free parameter LB models. In this platform, both the equilibrium distribution functions and associated lattice velocities are given from physical conservation laws.

In practical applications, there are some drawbacks for LBM [14], such as tie-up of mesh spacing and time intervals. In addition, since the boundary conditions are not directly applied and the lattice models are uniform, the standard LBM is usually limited to a uniform mesh with simple boundaries. To overcome the drawbacks of the standard LBM, an alternative method is to solve the discrete velocity Boltzmann equation (DVBE) with well-established numerical methods [15,16]. Solving the DVBE can eliminate the tie-up between time interval and mesh spacing of the standard LBM, but it also encounters problems such as poor numerical stability and large numerical dissipation [17,18]. Moreover, both the LBM and numerical methods for solving DVBE are memory intensive for simulation of multidimensional flows [19]. To avoid solving the lattice Boltzmann equation (LBE) and DVBE directly, Shu and his co-workers [20–23] proposed the lattice Boltzmann flux solver (LBFS) for simulation of single-component compressible flows. In LBFS, the Euler/Navier-Stokes (N-S) equations are discretized by the finite volume method and the numerical flux at the cell interface is evaluated by applying the local solution of one-dimensional LBE. Compared with other well-established computational fluid dynamics solvers, in LBFS, the numerical flux is evaluated by a virtual physical process. Moreover, LBFS is applied locally at each cell interface, and the streaming time step has nothing to do with the physical time step for evolution of the macroscopic variables. Therefore, LBFS can be effectively applied for complex geometry and unsteady flow simulation. Recently, LBFS is extended to simulate multiphase flow [21] and compressible viscous flow [22–25]. The existing LBFS considers both the equilibrium part and nonequilibrium part of the distribution function in evaluating the numerical flux at the cell interface. In order to capture strong shock waves, the influence of the nonequilibrium part of distribution function is treated as the numerical dissipation and controlled by a switch function. However, it is found that the existing LBFS has a high requirement for grid quality, and for simulation of multicomponent compressible viscous reacting flows, the numerical dissipation is still too large in the smooth region.

In this work, we extend the existing LBFS to simulate the multicomponent compressible viscous reacting flows. The inviscid flux is evaluated by multicomponent LBFS with the multicomponent non-free parameter D1Q4 model, while the viscous flux is calculated by the traditional central difference scheme. At first, the multicomponent non-free parameter D1Q4 model is derived from the conservation forms of moments. In this process, we can obtain the relationship between the inviscid flux of multicomponent Navier-Stokes equations and the distribution function. Like the existing LBFS, the distribution function at the cell interface consists of an equilibrium part and a nonequilibrium part. According to the Chapman-Enskog analysis, the equilibrium part corresponds to the inviscid flux and the nonequilibrium part can be viewed as the numerical dissipation. Given this, the numerical flux attributed to the equilibrium part should be dominant in the smooth region, while the numerical dissipation originating from the nonequilibrium part should be mainly added near the shock wave and combustion front for numerical stability. This requirement can be achieved by using a modified switch function, which considers the influence of the grid aspect ratio and combustion effect. To validate the developed solver, three different cases with a large temperature range, complex chemical reaction model, fast- and slow-reacting flow field, and complex geometry and flow field structure are simulated. The results of multicomponent LBFS are compared with those of the AUSM+ scheme [26] and reference data in the literature.

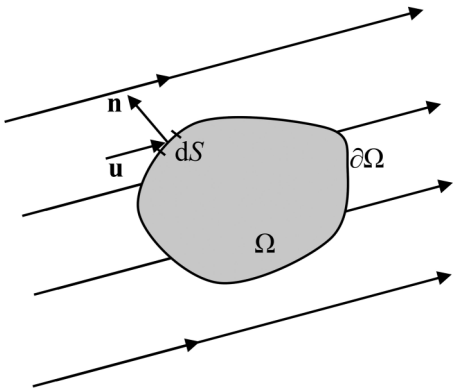

FIG. 1. Definition of a finite control volume (fixed in space).

II. MULTICOMPONENT NAVIER-STOKES EQUATIONS, MULTICOMPONENT NON-FREE PARAMETER D1Q4 MODEL, AND THEIR CONNECTIONS

A. Multicomponent Navier-Stokes equations

In this work, we solve the conserved Navier-Stokes (N-S) equations discretized by fixed control volume, which is shown in Fig. 1. The integral form of two-dimensional multicomponent force–free and heat source–free N-S equations [27] can be written as

$$\frac{\partial}{\partial t}\int_{\Omega}\mathbf{W}d\Omega+\oint_{\partial\Omega}(\mathbf{F}_c-\mathbf{F}_v)dS=\int_{\Omega}\mathbf{Q}d\Omega, \qquad (1)$$

where Ω is the control volume, $\partial\Omega$ is the surface of the control volume, and S is the area of the surface. In Eq. (1), the conservation laws of mass, momentum, and energy are applied to the conservative variables $\mathbf{W}$ to describe their variation of time in the fixed control volume Ω. The inviscid flux $\mathbf{F}_c$ and viscous flux $\mathbf{F}_v$ represent the amount of the conservative variables entering the control volume through the boundary dS with the influent velocity $\mathbf{u}$ and transport phenomena, respectively. The source term $\mathbf{Q}$ gives the mass change of each species caused by chemical reaction in the control volume [28].

The conservative variables $\mathbf{W}$, inviscid flux $\mathbf{F}_c$, viscous flux $\mathbf{F}_v$, and source term $\mathbf{Q}$ are given by

$$\mathbf{W}=\begin{bmatrix}\rho_1\\ \vdots\\ \rho_{NS}\\ \rho u\\ \rho v\\ \rho E\end{bmatrix},\quad \mathbf{F}_c=\begin{bmatrix}\rho_1 u_n\\ \vdots\\ \rho_{NS}u_n\\ \rho u u_n+n_x p\\ \rho v u_n+n_y p\\ (\rho E+p)u_n\end{bmatrix},\quad \mathbf{F}_v=\begin{bmatrix}n_x\Phi_{x,1}+n_y\Phi_{y,1}\\ \vdots\\ n_x\Phi_{x,NS}+n_y\Phi_{y,NS}\\ n_x\tau_{xx}+n_y\tau_{xy}\\ n_x\tau_{yx}+n_y\tau_{yy}\\ n_x\Theta_x+n_y\Theta_y\end{bmatrix},\quad \mathbf{Q}=\begin{bmatrix}\dot{\omega}_1\\ \vdots\\ \dot{\omega}_{NS}\\ 0\\ 0\\ 0\end{bmatrix}, \tag{2}$$

where NS is the number of species, and ρ_i and $\dot{\omega}_i$ are the density and net mass product rate of the ith species, respectively. p and ρ are the pressure and density of the mean flow. $\mathbf{u}=(u,v)$ and $\mathbf{n}=(n_x,n_y)$ are the velocity vector and unit normal vector in the Cartesian system, respectively. τ_{ij} denotes the components of the viscous stress tensor. The normal velocity u_n is defined as the product of velocity vector and unit normal vector as

$$u_n=\mathbf{u}\cdot\mathbf{n}=n_x u+n_y v. \tag{3}$$

The total energy of the mean flow E is defined as

$$\rho E=\sum_{i=1}^{NS}\rho_i h_i+\frac{1}{2}\rho(u^2+v^2)-p, \tag{4}$$

where h_i is the specific enthalpy of the ith species given by

$$h_i=\int_{T_0}^{T}c_{p,i}dT+h_i^0. \tag{5}$$

Here, the ${h_i}^0$ and $c_{p,i}$ are the specific enthalpy of formation at the reference temperature T_0 and specific heat at constant pressure of the ith species, respectively. T is the temperature of the mean flow. In the viscous flux $\mathbf{F}_v$, $\Phi_{i,j}$ is the term of species diffusion, and Θ_i represents the term describing the influence of viscous stress and heat conduction, which can be written as

$$\begin{aligned}\Phi_{x,i}&=\rho D_i\frac{\partial c_i}{\partial x}\\ \Phi_{y,i}&=\rho D_i\frac{\partial c_i}{\partial y},\end{aligned} \tag{6}$$

$$\begin{aligned}\Theta_x&=u\tau_{xx}+v\tau_{xy}+k\frac{\partial T}{\partial x}+\rho\sum_{i=1}^{NS}h_i D_i\frac{\partial c_i}{\partial x}\\ \Theta_y&=u\tau_{yx}+v\tau_{yy}+k\frac{\partial T}{\partial y}+\rho\sum_{i=1}^{NS}h_i D_i\frac{\partial c_i}{\partial y},\end{aligned} \tag{7}$$

where c_i and D_i are the mass fraction and mass diffusion coefficient of the ith species, respectively.

The equation of state can be written as

$$p=\sum_{i=1}^{NS}p_i=\sum_{i=1}^{NS}\rho_i\frac{R}{M_i}T, \tag{8}$$

where R is the universal gas constant and M_i is the molecular weight of the ith species.

In general, the chemical reaction can be written as [29]

$$\sum_{i=1}^{NJ}\alpha_{i,r}x_i\underset{k_{b,r}}{\overset{k_{f,r}}{\rightleftharpoons}}\sum_{i=1}^{NJ}\beta_{i,r}x_i, \tag{9}$$

where NJ is the total number of reacting species and catalytic bodies. $\alpha_{i,r}$ and $\beta_{i,r}$ are the stoichiometric coefficients of reactants and products of the ith species x_i in rth reactions, respectively. $k_{f,r}$ and $k_{b,r}$ are the forward and backward reaction rate of the rth reaction. The net mass production rate of the ith species is

$$\dot{\omega}_i=M_i\sum_{r=1}^{NR}(\beta_{i,r}-\alpha_{i,r})\left[k_{f,r}\prod_{j=1}^{NJ}(\gamma_j\rho)^{\alpha_{j,r}}-k_{b,r}\prod_{j=1}^{NJ}(\gamma_j\rho)^{\beta_{j,r}}\right], \tag{10}$$

where NR is the number of chemical reactions and γ is the mole mass ratio.

In this work, the chemical kinetic model is assumed to obey the modified Arrhenius equation as [30]

$$k=AT^n\exp\left(-\frac{E_a}{RT}\right), \tag{11}$$

where A is the pre-exponential factor, n is the temperature exponent, and E_a is the activation energy for the reaction. For the case that the backward reaction rate is not given explicitly, it can be computed by using the local chemical equilibrium constant.

B. Multicomponent non-free parameter D1Q4 lattice Boltzmann model

Inspired by the work of Yang *et al.* [13], which develops a non-free parameter D1Q4 model for simulation of single-component compressible viscous flows, a multicomponent non-free parameter D1Q4 model is developed in this work. The distribution of discrete equilibrium states and particle velocities for this model is illustrated in Fig. 2, which contains four equilibrium density distribution functions g_1, g_2, g_3, g_4 and two lattice velocities d_1, d_2.

This model is derived from the Bhatnagar-Gross-Krook (BGK) type Boltzmann equation with a Maxwellian distribution function. Since this D1Q4 model is only used for

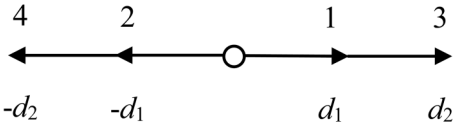

FIG. 2. The discrete particle velocity of multicomponent non-free parameter D1Q4 model.

calculating the inviscid flux along the normal direction of the cell interface, one-dimensional multicomponent Euler equations need to be recovered by the multicomponent non-free parameter D1Q4 model. In particular, the following relations must be fulfilled [23]:

$$\begin{aligned}
\rho &= \sum_{j=1}^{4} g_j \\
\rho u &= \sum_{j=1}^{4} g_j \xi_j \\
\rho uu + p &= \sum_{j=1}^{4} g_j \xi_j \xi_j \\
\rho E &= \sum_{j=1}^{4} g_j \left(\frac{1}{2} \xi_j \xi_j + e_p \right) \\
(\rho E + p)u &= \sum_{j=1}^{4} g_j \left(\frac{1}{2} \xi_j \xi_j + e_p \right) \xi_j,
\end{aligned} \tag{12}$$

where g_j and ξ_j are the equilibrium density distribution function and lattice velocity, respectively, of the particle j, and u is the velocity of the mean flow. The densities of different species are expressed by their mass fractions:

$$\rho_i = c_i \rho = c_i \sum_{j=1}^{4} g_j. \tag{13}$$

By substituting the first and the third relations into the fourth relation of Eq. (12) and using Eq. (4), the particle potential energy e_p can be expressed by

$$e_p = \frac{\sum_{i=1}^{NS} \rho_i h_i}{\rho} - \frac{3p}{2\rho}. \tag{14}$$

Let us introduce the peculiar velocity of particles as

$$c = \sqrt{\frac{p}{\rho}}. \tag{15}$$

Substituting Eqs. (14) and (15) into Eq. (12) and setting $\xi_1 = d_1, \xi_2 = -d_1, \xi_3 = d_2$, and $\xi_4 = -d_2$, we can get four reduced relations:

$$\begin{aligned}
\rho &= g_1 + g_2 + g_3 + g_4 \\
\rho u &= g_1 d_1 - g_2 d_1 + g_3 d_2 - g_4 d_2 \\
\rho u^2 + p &= g_1 d_1^2 + g_2 d_1^2 + g_3 d_2^2 + g_4 d_2^2 \\
\rho u^3 + 3c^2 u &= g_1 d_1^3 - g_2 d_1^3 + g_3 d_2^3 - g_4 d_2^3.
\end{aligned} \tag{16}$$

It can be seen that the term of particle potential energy e_p and enthalpy h in the fourth relation of Eq. (16) is eliminated. By solving Eq. (16), g_i can be expressed as

$$\begin{aligned}
g_1 &= \frac{\rho\left(c^2 d_1 + 3c^2 u - d_1 d_2^2 + d_1 u^2 - d_2^2 u + u^3\right)}{2d_1\left(d_1^2 - d_2^2\right)} \\
g_2 &= \frac{\rho\left(c^2 d_1 - 3c^2 u - d_1 d_2^2 + d_1 u^2 + d_2^2 u - u^3\right)}{2d_1\left(d_1^2 - d_2^2\right)} \\
g_3 &= -\frac{\rho\left(c^2 d_2 + 3c^2 u - d_1^2 d_2 + d_2 u^2 - d_1^2 u + u^3\right)}{2d_2\left(d_1^2 - d_2^2\right)} \\
g_4 &= -\frac{\rho\left(c^2 d_2 - 3c^2 u - d_1^2 d_2 + d_2 u^2 + d_1^2 u - u^3\right)}{2d_2\left(d_1^2 - d_2^2\right)}.
\end{aligned} \tag{17}$$

In this work, only inviscid flux is reconstructed by using this D1Q4. Furthermore, in order to obtain a non-free parameter D1Q4 model, which is more stable and robust for solving compressible problems, the particle velocities d_1 and d_2 are evaluated by the higher-order moments for recovering the N-S equations and the Burnett correction to heat flux as follows:

$$\begin{aligned}
\rho u^4 + 6\rho c^2 u^2 + 3\rho c^4 &= g_1 d_1^4 + g_2 d_1^4 + g_3 d_2^4 + g_4 d_2^4 \\
\rho u^5 + 10\rho c^2 u^3 + 15\rho c^4 u &= g_1 d_1^5 - g_2 d_1^5 + g_3 d_2^5 - g_4 d_2^5.
\end{aligned} \tag{18}$$

By solving Eq. (18), we can get

$$\begin{aligned}
d_1 &= \sqrt{u^2 + 3c^2 - \sqrt{4u^2 c^2 + 6c^4}} \\
d_2 &= \sqrt{u^2 + 3c^2 + \sqrt{4u^2 c^2 + 6c^4}}.
\end{aligned} \tag{19}$$

C. Connections of multicomponent Navier-Stokes equations and multicomponent non-free parameter D1Q4 model

In order to apply the multicomponent non-free parameter D1Q4 model to evaluate the inviscid flux $\mathbf{F}_c$, the relations between distribution functions and conservative variables as well as inviscid flux must be obtained. Since the multicomponent non-free parameter D1Q4 model is applied along the normal direction of the cell interface as shown in Fig. 3, the conservative variables $\mathbf{W}$ and inviscid flux $\mathbf{F}_c$ are needed to be transformed from one-dimensional conservative variables $\bar{\mathbf{W}}$ and inviscid flux $\bar{\mathbf{F}}_c$ to a two-dimensional global coordinate system.

According to Eq. (12), the conservative variables $\bar{\mathbf{W}}$ and inviscid flux $\bar{\mathbf{F}}_c$ attributed to the normal velocity on the surface S can be calculated by the multicomponent non-free parameter D1Q4 model as follows:

$$\bar{\mathbf{W}} = \begin{bmatrix} \rho_1 \\ \vdots \\ \rho_{NS} \\ \rho u_n \\ \rho\left(e + u_n^2/2\right) \end{bmatrix} = \sum_{j=1}^{4} \boldsymbol{\varphi}_a f_j(\mathbf{r}, t), \tag{20}$$

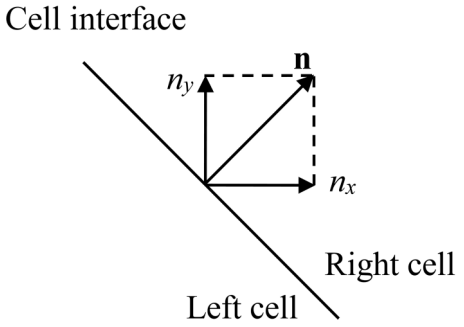

FIG. 3. Local coordinate system at the cell interface.

$$\bar{\mathbf{F}}_c = \begin{bmatrix} \rho_1 u_n \\ \vdots \\ \rho_{NS} u_n \\ \rho u_n^2 + p \\ \left[\rho\left(e + u_n^2/2\right) + p\right] u_n \end{bmatrix} = \sum_{j=1}^{4} \xi_j \boldsymbol{\varphi}_a f_j(\mathbf{r}, t), \quad (21)$$

where e is the internal energy. The location $\mathbf{r}$ denotes the midpoint of the cell interface and t represents the current time level. $\boldsymbol{\varphi}_a$ stands for

$$\boldsymbol{\varphi}_a = \begin{bmatrix} c_1 \\ \vdots \\ c_{NS} \\ \xi_j \\ \xi_j^2/2 + e_p \end{bmatrix}. \quad (22)$$

The velocity components in the Cartesian coordinate system can be expressed by normal velocity and tangential velocity as

$$\begin{aligned} u &= n_x u_n - n_y u_\tau \\ v &= n_x u_\tau + n_y u_n. \end{aligned} \quad (23)$$

Using Eqs. (2), (20), (21), and (23), the conservative variables $\mathbf{W}$ and inviscid flux $\mathbf{F}_c$ can be expressed by $\bar{\mathbf{W}}$ and $\bar{\mathbf{F}}_c$ as follows:

$$\mathbf{W} = \begin{bmatrix} \rho_1 \\ \vdots \\ \rho_{NS} \\ \rho(n_x u_n - n_y u_\tau) \\ \rho(n_x u_\tau + n_y u_n) \\ \rho\left(e + u_n^2/2\right) + \rho u_\tau^2/2 \end{bmatrix} = \begin{bmatrix} \bar{\mathbf{W}}(1) \\ \vdots \\ \bar{\mathbf{W}}(NS) \\ \bar{\mathbf{W}}(NS+1) n_x - \rho u_\tau n_y \\ \bar{\mathbf{W}}(NS+1) n_y + \rho u_\tau n_x \\ \bar{\mathbf{W}}(NS+2) + \rho u_\tau^2/2 \end{bmatrix}, \quad (24)$$

$$\mathbf{F}_c = \begin{bmatrix} \rho_1 u_n \\ \vdots \\ \rho_{NS} u_n \\ \left(\rho u_n^2 + p\right) n_x - \rho u_n u_\tau n_y \\ \left(\rho u_n^2 + p\right) n_y + \rho u_n u_\tau n_x \\ \left[\rho\left(e + u_n^2/2\right) + p\right] u_n + \rho u_n u_\tau^2/2 \end{bmatrix} = \begin{bmatrix} \bar{\mathbf{F}}_c(1) \\ \vdots \\ \bar{\mathbf{F}}_c(NS) \\ \bar{\mathbf{F}}_c(NS+1) n_x - \rho u_n u_\tau n_y \\ \bar{\mathbf{F}}_c(NS+1) n_y + \rho u_n u_\tau n_x \\ \bar{\mathbf{F}}_c(NS+2) + \rho u_n u_\tau^2/2 \end{bmatrix}. \quad (25)$$

As for the tangential velocity and the flux attributed to the tangential velocity at the cell interface, an approximate methodis adopted, which will be given in the next section.

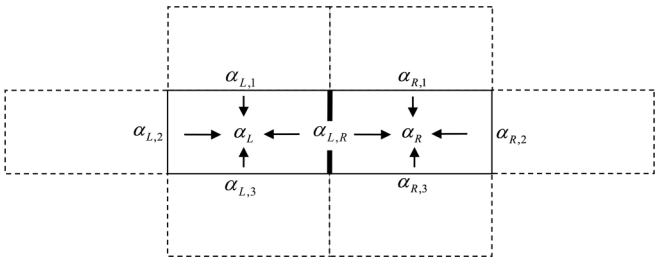

FIG. 4. The switch function calculation process.

III. LATTICE BOLTZMANN FLUX SOLVER FOR MULTICOMPONENT VISCOUS COMPRESSIBLE REACTING FLOWS

The key of the multicomponent LBFS is to evaluate the inviscid flux $\mathbf{F}_c$ and introduce appropriate numerical dissipation in the flow field. In multicomponent reacting flows, it is also important to calculate the internal energy and densities of different species in the gas mixture. In the present multicomponent LBFS, both the equilibrium part and nonequilibrium part of the distribution function are considered. The equilibrium part is used to obtain an accurate result in the smooth region, while the nonequilibrium part is added near the shock wave and combustion front to provide enough numerical dissipation for stability. As shown in the work of Yang *et al.* [13], the total inviscid flux at the cell interface can be written as

$$\mathbf{F}_{c,i+1/2} = \mathbf{F}^I_{c,i+1/2} + \tau_0\left(\mathbf{F}^{II}_{c,i+1/2} - \mathbf{F}^I_{c,i+1/2}\right), \quad (26)$$

where τ_0 is the dimensionless collision time, $\mathbf{F}^I_{c,i+1/2}$ is the inviscid flux attributed to the equilibrium part of the distribution function at the cell interface, while the $\mathbf{F}^{II}_{c,i+1/2} - \mathbf{F}^I_{c,i+1/2}$ represents the contribution of the nonequilibrium part.

A. Evaluation of $\mathbf{F}^I_{c,i+1/2}$

As $\mathbf{F}^I_{c,i+1/2}$ is the contribution of the equilibrium distribution function at the cell interface, we need to compute the conservative variables $\bar{\mathbf{W}}$ at the same location in advance. Since the non-free parameter D1Q4 model is used to describe the total density of the gas mixture, as shown in Eq. (13), the densities of different species at the cell interface are computed by the distribution functions and the mass fraction of the left and right cells as

$$\rho_i = \sum_{j=1}^{4} g_j c_i = \sum_{j=1,3} g_j^L c_i^L + \sum_{j=2,4} g_j^R c_i^R. \quad (27)$$

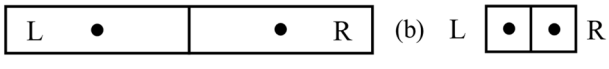

FIG. 5. The different aspect ratios of the grid with (a) large aspect ratio and (b) unit aspect ratio.

Substituting Eqs. (22) and (27) into Eq. (20), the conservative variables $\bar{\mathbf{W}}$ can be written as

$$\bar{\mathbf{W}}_{i+1/2} = \begin{bmatrix} \sum_{j=1,3} g_j c_1 \\ \vdots \\ \sum_{j=1,3} g_j c_{NS} \\ \sum_{j=1,3} g_j \xi_j \\ \sum_{j=1,3} g_j \frac{1}{2}(\xi_j \xi_j + e_p) \end{bmatrix}^L + \begin{bmatrix} \sum_{j=2,4} g_j c_1 \\ \vdots \\ \sum_{j=2,4} g_j c_{NS} \\ \sum_{j=2,4} g_j \xi_j \\ \sum_{j=2,4} g_j \frac{1}{2}(\xi_j \xi_j + e_p) \end{bmatrix}^R. \tag{28}$$

The distribution functions and particle velocities with subscript of 1 and 3 are taken from the left side of the cell interface, while variables with subscript of 2 and 4 are taken from the right side. The total density ρ and normal velocity u_n on the cell interface can be obtained easily by using the conservative variables in Eq. (28). However, there exists a problem of how to calculate the pressure at the cell interface. In Eq. (4), the enthalpies of different species are the function of temperature, so the pressure cannot be expressed in an explicit form. To calculate the pressure, the temperature at the cell interface should be determined in advance. Here we use the Newton iteration to estimate the value of temperature [31]. The function of temperature can be obtained by substituting Eq. (8) into Eq. (4) as

$$f(T) = \sum_{i=1}^{NS} \rho_i h_i + \frac{1}{2}\rho(u^2 + v^2) - \sum_{i=1}^{NS} \rho_i R_i T - \rho E = 0. \tag{29}$$

The Newton iteration of the temperature function can be written as

$$T^{(n+1)} = T^{(n)} - \frac{f(T^{(n)})}{f'(T^{(n)})}, \tag{30}$$

where

$$f'(T^{(n)}) = \sum_{i=1}^{NS} \rho_i c_{p,i} - \sum_{i=1}^{NS} \rho_i R_i. \tag{31}$$

As a result, the approximate value of temperature in the next step can be calculated by

$$T^{(n+1)} = T^{(n)} - \frac{\sum_{i=1}^{NS} \rho_i h_i + \frac{1}{2}\rho(u^2 + v^2) - \sum_{i=1}^{NS} \rho_i R_i T^{(n)} - \rho E}{\sum_{i=1}^{NS} \rho_i c_{p,i} - \sum_{i=1}^{NS} \rho_i R_i}. \tag{32}$$

Equation (32) can be further simplified as

$$T^{(n+1)} = \frac{\sum_{i=1}^{NS} \rho_i (c_{p,i} T^{(n)} - h_i) - \frac{1}{2}\rho(u^2 + v^2) + \rho E}{\sum_{i=1}^{NS} \rho_i c_{v,i}}, \tag{33}$$

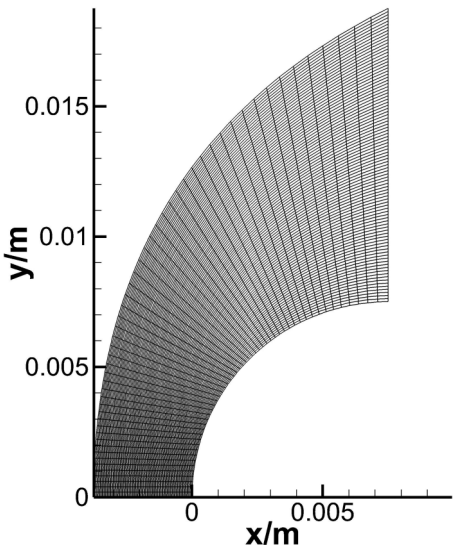

FIG. 6. Computational domain for shock-induced combustion flow.

where $c_{v,i}$ is the specific heat at constant volume. The initial value of temperature $T^{(0)}$ is given by the Roe average of left and right cells, and $c_{p,i}$, $c_{v,i}$, h_i in step n are approximated by using $T^{(n-1)}$. To most cells, 2 or 3 times of Newton iteration is sufficient for reaching the convergence criterion of 1.0×10^{-8}. Once the temperature is obtained, the pressure can be computed straightforwardly by using Eq. (8).

As described in Sec. II C, the non-free parameter D1Q4 model is applied only in the normal direction of the cell interface. Therefore, the tangential velocity at the cell interface is estimated by

$$\begin{aligned} \rho u_\tau &= \sum_{j=1}^{4} g_j u_\tau = \sum_{j=1,3} g_j^L u_\tau^L + \sum_{j=2,4} g_j^R u_\tau^R \\ \rho u_\tau^2 &= \sum_{j=1}^{4} g_j (u_\tau)^2 = \sum_{j=1,3} g_j^L \left(u_\tau^L\right)^2 + \sum_{j=2,4} g_j^R \left(u_\tau^R\right)^2. \end{aligned} \tag{34}$$

It is convenient to calculate $\mathbf{F}^I_{c,i+1/2}$ by directly using the value of $\bar{\mathbf{W}}$ as follows:

$$\mathbf{F}^I_{c,i+1/2} = \begin{bmatrix} \bar{W}(1) u_n \\ \vdots \\ \bar{W}(NS) u_n \\ [\bar{W}(NS+1) u_n + p] n_x - \bar{W}(NS+1) u_\tau n_y \\ [\bar{W}(NS+1) u_n + p] n_y + \bar{W}(NS+1) u_\tau n_x \\ \left[\bar{W}(NS+2) + p + \frac{1}{2}\rho u_\tau^2\right] u_n \end{bmatrix}_{i+1/2}. \tag{35}$$

B. Evaluation of $\mathbf{F}^{II}_{c,i+1/2}$

$\mathbf{F}^{II}_{c,i+1/2}$ is the contribution of equilibrium distribution function around the cell interface. The same as described before Eqs. (27) and (34), the numerical flux attributed to the

TABLE I. Chemistry model from Moretti [37].

No.	Reaction
1	$O_2 + H = OH + O$
2	$H_2 + O = OH + H$
3	$H_2 + OH = H_2O + H$
4	$OH + OH = H_2O + O$
5	$OH + H + M = H_2O + M$
6	$H + H + M = H_2 + M$
7	$O + H + M = OH + M$
8	$O + O + M = O_2 + M$

tangential velocity in $\mathbf{F}^{II}_{c,i+1/2}$ is calculated in the same way as in $\mathbf{F}^{I}_{c,i+1/2}$, i.e.,

$$\rho u_n u_\tau = \sum_{j=1}^{4} g_j \xi_j u_\tau = \sum_{j=1,3} g_j^L \xi_j^L u_\tau^L + \sum_{j=2,4} g_j^R \xi_j^R u_\tau^R, \tag{36}$$

$$\rho u_n u_\tau^2 = \sum_{j=1}^{4} g_j \xi_j u_\tau^2 = \sum_{j=1,3} g_j^L \xi_j^L \left(u_\tau^L\right)^2 + \sum_{j=2,4} g_j^R \xi_j^R \left(u_\tau^R\right)^2. \tag{37}$$

Finally, $\mathbf{F}^{II}_{c,i+1/2}$ can be calculated by using Eqs. (25), (36), and (37) as follows:

$$\mathbf{F}^{II}_{c,i+1/2} = \begin{bmatrix} \sum_{j=1,3} g_j \xi_j c_1 \\ \vdots \\ \sum_{j=1,3} g_j \xi_j c_{NS} \\ \sum_{j=1,3} g_j \xi_j \xi_j n_x - \sum_{j=1,3} g_j \xi_j u_\tau n_y \\ \sum_{j=1,3} g_j \xi_j \xi_j n_y + \sum_{j=1,3} g_j \xi_j u_\tau n_x \\ \sum_{j=1,3} g_j \xi_j \left(\frac{1}{2}\xi_j \xi_j + e_p\right) + \frac{1}{2}\sum_{j=1,3} g_j \xi_j u_\tau^2 \end{bmatrix}^L + \begin{bmatrix} \sum_{j=2,4} g_j \xi_j c_1 \\ \vdots \\ \sum_{j=2,4} g_j \xi_j c_{NS} \\ \sum_{j=2,4} g_j \xi_j \xi_j n_x - \sum_{j=2,4} g_j \xi_j u_\tau n_y \\ \sum_{j=2,4} g_j \xi_j \xi_j n_y + \sum_{j=2,4} g_j \xi_j u_\tau n_x \\ \sum_{j=2,4} g_j \xi_j \left(\frac{1}{2}\xi_j \xi_j + e_p\right) + \frac{1}{2}\sum_{j=2,4} g_j \xi_j u_\tau^2 \end{bmatrix}^R. \tag{38}$$

TABLE II. Free stream conditions for shock-induced combustion flow.

			Mass fraction		
Ma	P (Pa)	T (K)	c (N_2)	c (O_2)	c (H_2)
6.9765	42262	250	0.74519	0.22650	0.02831

TABLE III. References of simulation parameters for shock-induced combustion flow.

Parameters	Boundary conditions	Chemical kinetics model	Thermodynamic database
Reference	[39]	[37]	[38]

C. Control of numerical dissipation

In Eq. (26), if $\tau_0 = 0$, the numerical dissipation from the nonequilibrium part of the distribution function at the cell interface vanishes and an accurate result can be obtained. However, the numerical dissipation is needed to capture strong shock waves. If $\tau_0 = 1$, the numerical dissipation is enabled at the whole computational domain, which is too large to get an accurate result in the smooth region. In the existing LBFS, a switch function is introduced to solve this problem.

The original form of the switch function at the cell interface is defined by [23]

$$\alpha = \tanh\left(C\frac{|p_L - p_R|}{p_L + p_R}\right), \tag{39}$$

where $\tanh(x)$ is the hyperbolic tangent function, and p_L and p_R are the pressure at the left and right sides of the cell interface. C is a positive amplification factor. For simulation of supersonic and hypersonic flows, to get a smooth switch function distribution, it is better to consider the effect of the cells around the interface shown in Fig. 4 as

$$\alpha^* = \max\{\alpha_L, \alpha_R\}, \tag{40}$$

where α_L and α_R are the maximum value of the switch function in the left and right cells as

$$\begin{aligned} \alpha_L &= \max_{i=1,N_{f,L}} \{\alpha_i\} \\ \alpha_R &= \max_{i=1,N_{f,R}} \{\alpha_i\}, \end{aligned} \tag{41}$$

where $N_{f,L}$ and $N_{f,R}$ are the number of faces of the left and right cells, respectively.

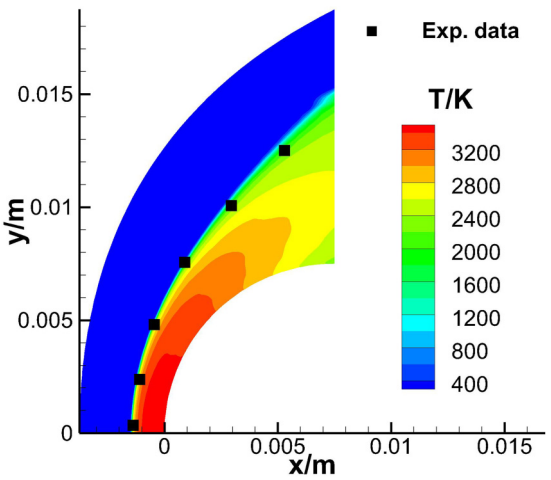

FIG. 7. Temperature contours with shock wave detachment distance.

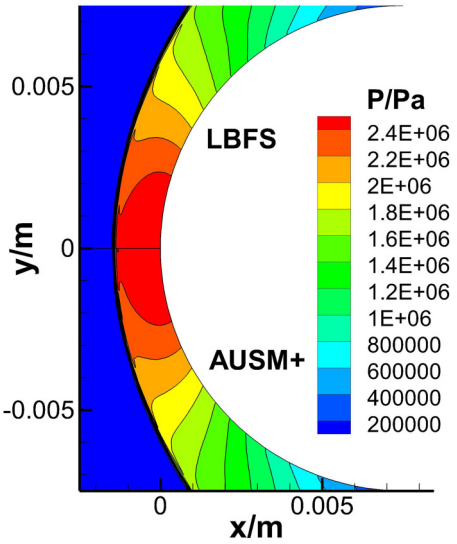

FIG. 8. Comparison of pressure contours by using different schemes.

The switch function in Eq. (39) encounters some problems on the nonuniform grid. If we suppose that there exists a uniform pressure gradient in the computational domain, there should exist a uniform numerical dissipation. However, as shown in Fig. 5(a), a larger aspect ratio of the grid will lead to a larger value of switch function at the shorter cell interface and then a larger numerical dissipation, which is unreasonable. In numerical simulation, the computational domain is not always uniform. For example, the grid in the boundary layer usually has a very large ratio of length and width for body-fitted grids, and sometimes the numerical scheme requires a large aspect ratio to add additional numerical viscosity [32]. Thus, it is hard to use the original switch function to solve the fluid flow problem with complex geometry, in which the aspect ratio of the grid is extremely high.

To overcome this defect, the effect of aspect ratio of the grid should be considered. For the two-dimensional case, a

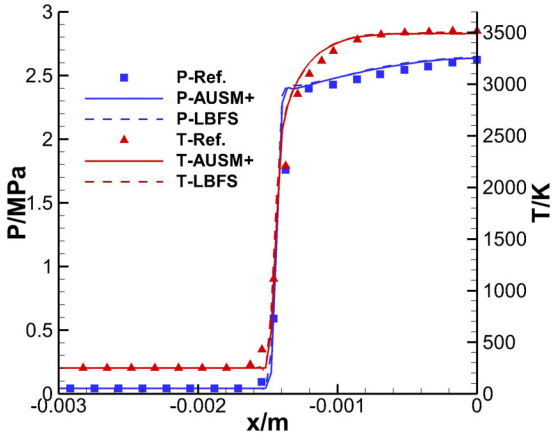

FIG. 9. Pressure and temperature profiles along the stagnation line.

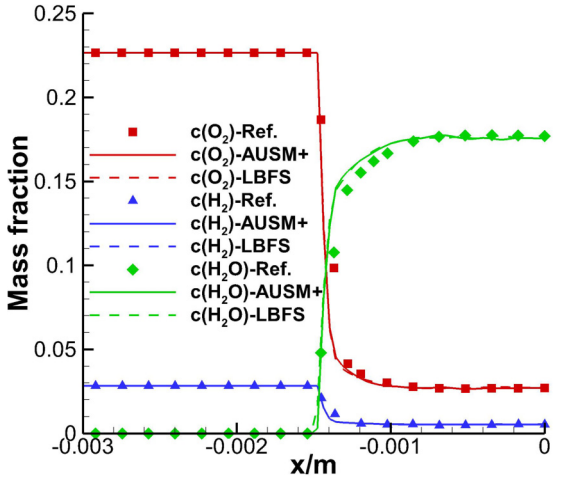

FIG. 10. Mass fractions of main species profiles along the stagnation line.

grid parameter r is used to evaluate the aspect ratio:

$$r = \begin{cases} \min\left(1.0, \frac{\bar{\Omega}}{L_{L,R}^2}\right), & \text{for quadrilateral grid} \\ \min\left(1.0, \frac{2\bar{\Omega}}{L_{L,R}^2}\right), & \text{for triangle grid} \end{cases}, \tag{42}$$

where $\bar{\Omega}$ is the average volume of the left and right cells, and $L_{L,R}^2$ is the square of distance between the left and right cell centers. The minimum function is used to guarantee that only the switch function on the short edge of the cell interface is modified. This method means that the value of the switch function at the cell interface is normalized based on the long edge of both cells.

Considering the chemical reaction in the flow field, i.e., the combustion front is not always at the same location as the shock wave, the numerical dissipation should be introduced to both the shock wave and the combustion front. Thus, the switch function in Eq. (39) is written in a modified form as

$$\alpha = \tanh\left[rC\max\left(\frac{|p_L - p_R|}{p_L + p_R}, \frac{|T_L - T_R|}{T_L + T_R}\right)\right]. \tag{43}$$

As shown in Eqs. (39) and (43), another factor for calculation of the switch function is the overall size of the grid, which is represented by the positive amplification factor C. A grid with small size or large aspect ratio needs a large value of C. Finally, the total inviscid flux at the cell interface in Eq. (26) can be written as

$$\mathbf{F}_{c,i+1/2} = (1-\alpha^*)\mathbf{F}^I_{c,i+1/2} + \alpha^*\mathbf{F}^{II}_{c,i+1/2}. \tag{44}$$

TABLE IV. Comparison of computational efficiency for different schemes.

Time	AUSM+	LBFS	Comparison
Average time cost per step (s)	0.09605	0.10248	6.69%
Convergence time consumption (s)	2326.73	1946.24	−16.35%

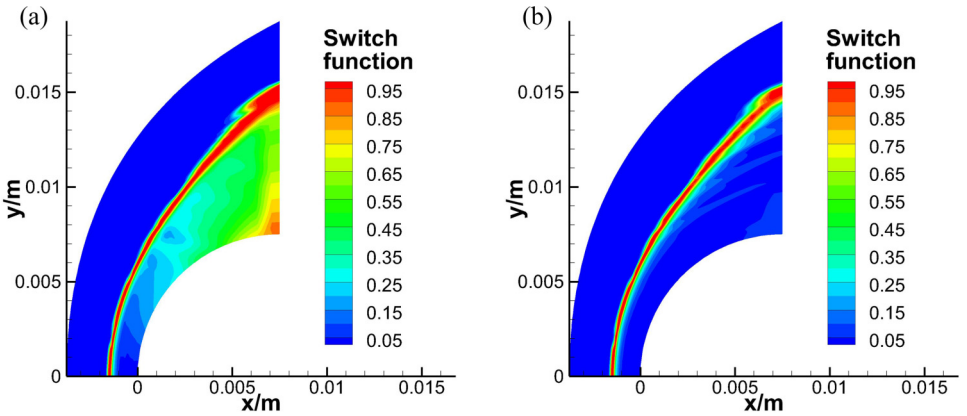

FIG. 11. Comparison of switch function contours: (a) without grid modification and (b) with grid modification.

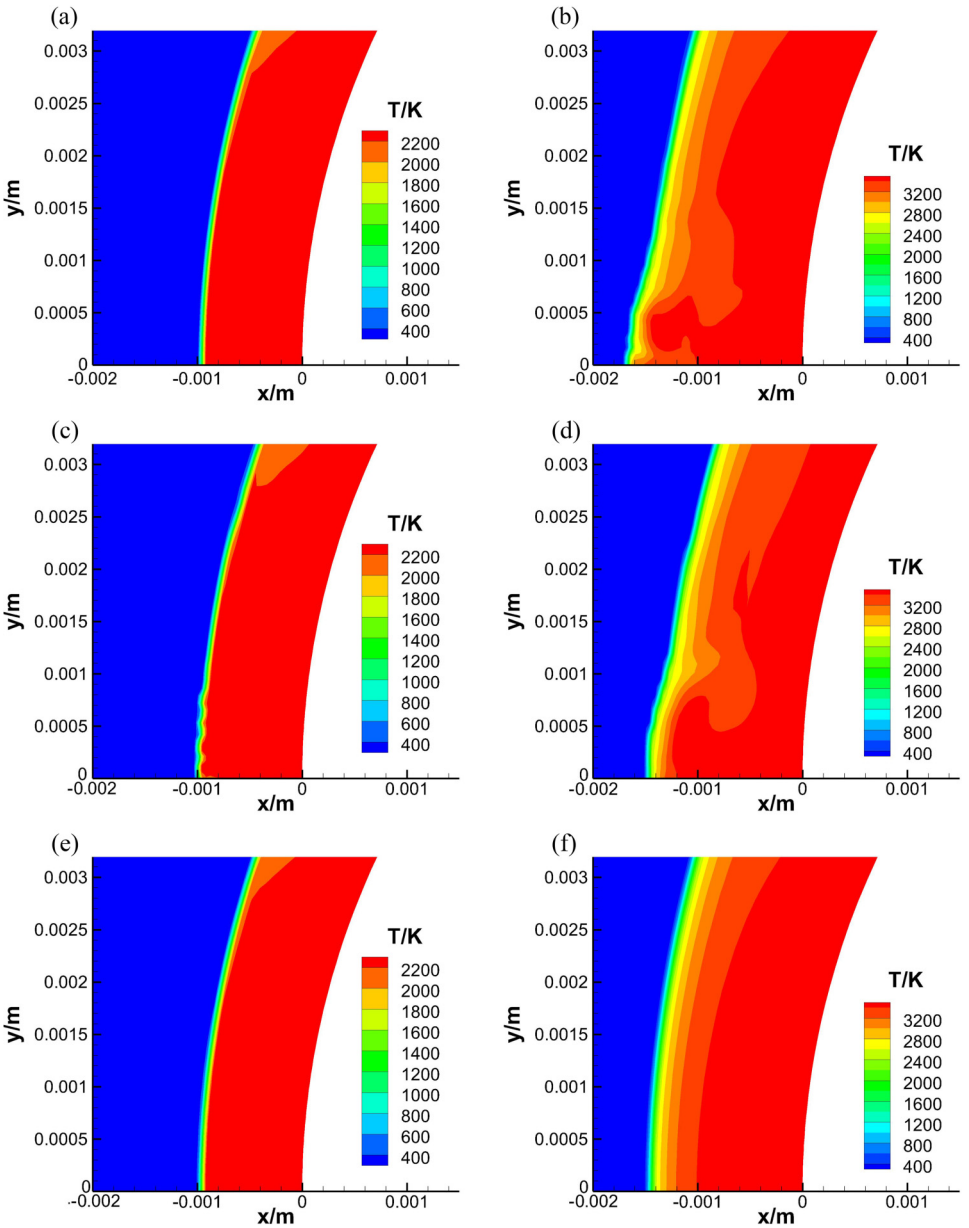

FIG. 12. Comparison of temperature contours near the symmetric axis by using different schemes: (a) Roe scheme without chemical reaction, (b) Roe scheme with chemical reaction, (c) AUSM+ scheme without chemical reaction, (d) AUSM+ scheme with chemical reaction, (e) LBFS without chemical reaction, and (f) LBFS with chemical reaction.

TABLE V. Chemistry model from Gupta [45].

No.	Reaction
1	$O_2 + M = 2O + M$
2	$N_2 + M = 2N + M$
3	$NO + M = N + O + M$
4	$N_2 + O = NO + N$
5	$NO + O = O_2 + N$
6	$N_2 + N = 2N + N$
7	$N + O = NO^+ + e^-$

D. Computational sequence

The basic solution procedure of the present solver can be outlined below:

(1) Reconstruct the conservative variables at two sides of the cell interface.

(2) Predict the conservative variables at the cell interface by Roe average.

(3) Use Eqs. (17) and (19) to calculate the equilibrium distribution function g_1, g_2, g_3, g_4 and lattice velocity d_1, d_2 at the left and right sides of the cell interface.

(4) Compute the inviscid flux $\mathbf{F}^I_{c,i+1/2}$ and $\mathbf{F}^{II}_{c,i+1/2}$ by Eqs. (35) and (38).

(5) Compute the switch function and the total inviscid flux across the cell interface $\mathbf{F}_{c,i+1/2}$ by Eqs. (43) and (44).

(6) Calculate the viscous flux $\mathbf{F}_{v,i+1/2}$ in Eq. (2) using the central difference method.

(7) Solve Eq. (1) using the explicit five-step Runge-Kutta method [33], which gives the conservative variables at cell centers at a new time level.

(8) Repeat steps (1)–(7) until the converged solution is achieved.

IV. NUMERICAL EXAMPLES

In order to validate the present multicomponent LBFS, three cases of compressible reacting flows are simulated in this section. In the simulation, the explicit five-step Runge-Kutta method is used for time advancing, and the piecewise linear reconstruction [34] with Venkatakrishnan's limiter [35] is adopted to reconstruct the conservative variables at two sides of the cell interface. All the computations were done on a personal computer with Intel Core i7-8750H CPU @ 2.20 GHz.

A. Shock-induced combustion flow

The first case is premixed stoichiometric hydrogen-air around a sphere with a diameter of 15 mm, which is taken from Lehr's experiment [36]. The high robustness and accuracy are required in the simulation since the chemical reactions occur very fast within a short distance. The computational domain shown in Fig. 6 is discretized by a structured grid with 95×55 cells, and the value of positive amplification factor C is taken as 15. Euler equations are solved in this case, and Moretti's chemistry model [37], which includes seven species (N_2, O_2, H_2, O, H, OH, and H_2O) and eight reactions, as listed in Table I, is used. As the temperature range in this case is below 5000 K, we use the same calculation method and physical properties database of CHEMKIN [38] to evaluate the transport properties of each species and gas mixture.

TABLE VI. Free stream conditions for hypersonic air chemical nonequilibrium flow.

			Mass fraction	
Ma	p (Pa)	T (K)	$c(N_2)$	$c(O_2)$
15.3	664	293	0.77	0.23

TABLE VII. Reference of simulation parameters for hypersonic air chemical nonequilibrium flow.

Parameters	Boundary conditions	Chemical kinetics model	Thermodynamic database
Reference	[46]	[45]	[45]

The free stream conditions are listed in Table II, and the mole ratio of different species in the premixed free stream is $N_2 : O_2 : H_2 = 3.76 : 1 : 2$. The adiabatic and noncatalytic condition is used for the wall, and the nonreflecting condition is utilized for the far field. The axisymmetric boundary is used along the line $y = 0$ m. All of the references of simulation parameters are listed in Table III.

Figure 7 shows the computed temperature contours and the shock wave detachment distance extracted from an experiment shadowgraph [36]. As shown in the figure, the bow shock location obtained by the multicomponent LBFS is in good agreement with the experimental data. Figure 8 compares the pressure contours computed by the multicomponent LBFS (upper) and AUSM+ scheme (lower). Clearly, no significant difference is found between these two results.

The comparison of pressure and temperature profiles along the stagnation line calculated by different schemes is shown

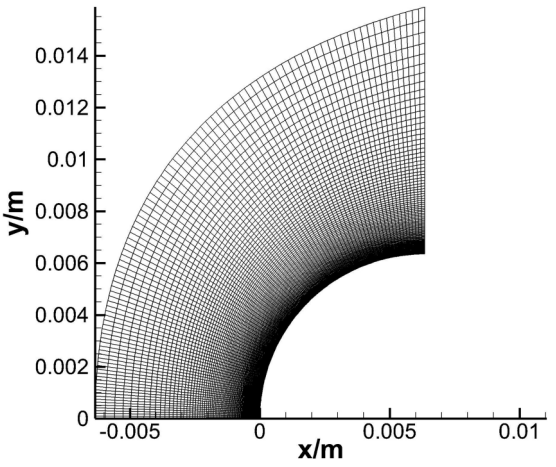

FIG. 13. Computational domain for hypersonic air chemical nonequilibrium flow.

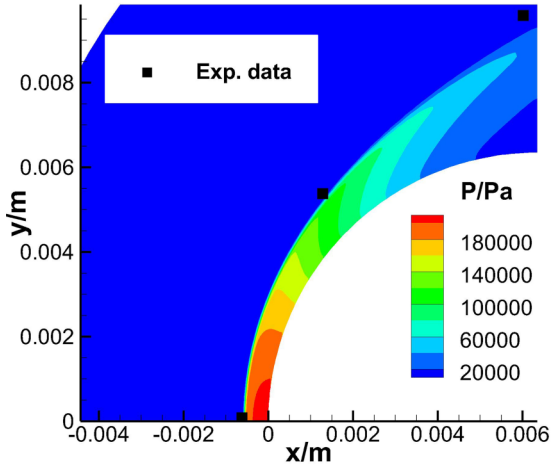

FIG. 14. Pressure contours with shock wave detachment distance.

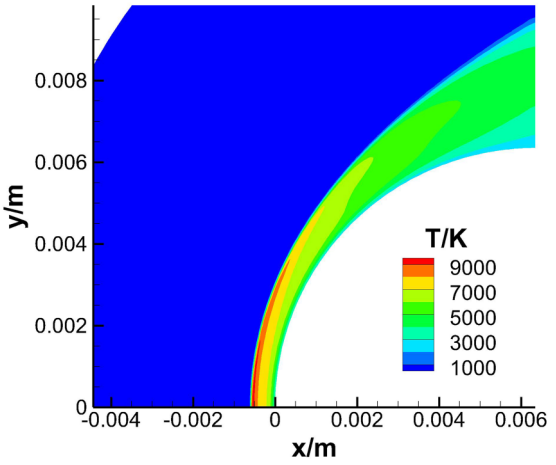

FIG. 16. Temperature contours of hypersonic air chemical nonequilibrium flow.

in Fig. 9. The ZND (Zeldovich, Neumann, and Doering) detonation theory [40] indicates that the leading shock wave compresses and heats the combustible gas mixture to its spontaneous combustion state. There exists a reacting zone after the compressing wave, where the chemical reactions occur and the pressure and temperature increase to their maximum values. For the leading detonation wave, there exists a Von Neumann spike. This spike occurs because the isobaric combustion cannot be maintained due to severe combustion and energy release after the shock wave. In Fig. 9, the Von Neumann spike is well captured in the pressure profile. Moreover, the results of the multicomponent LBFS and AUSM+ scheme are close to each other, and they agree well with the computational results from Ref. [39]. Figure 10 shows the mass fractions of different species along the stagnation line. It can be seen that the reaction occurs very fast in a narrow area after the shock wave. Once again, the results of multicomponent LBFS match well with those of the AUSM+ scheme and the reference data [39]. It is noted that because a refined mesh is used in the calculation, the drastic change near the bow shock can be seen more clearly than the reference data. As seen here, the accuracy and robustness of the multicomponent LBFS are well demonstrated.

The computational efficiency of the AUSM+ scheme and the present solver is listed in Table IV. Since it is hard to reach a good convergence level for reacting cases, we chose the density residual 1.0×10^{-3} as the convergence criterion. As we can see, even though the present solver has a higher average time cost per step by 6.69%, the convergence time cost is reduced by 16.35%. The good convergence property of the present solver is well demonstrated.

Next we show the effectiveness of Eq. (42) proposed in this work. Figure 11 shows a comparison of switch function contours with and without grid modification. Focusing on the value of switch function at the downstream of the bow shock, in Fig. 11(a) it can be seen that the value is extremely high while in Fig. 11(b) it is almost zero. Therefore, the effect of grid aspect ratio on the switch function can be removed effectively, which makes the developed multicomponent LBFS be more applicable to complex grids.

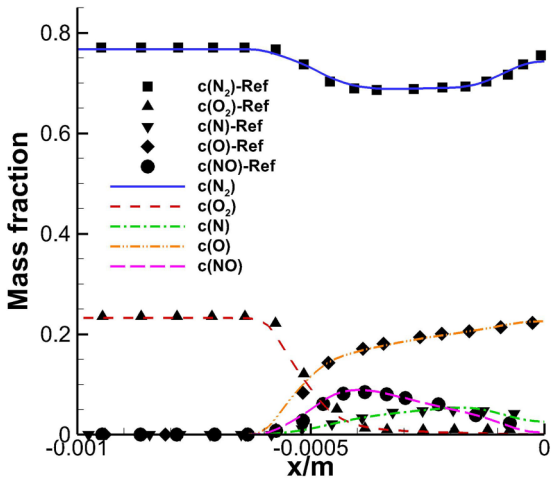

FIG. 15. Mass fractions of different species along the centerline.

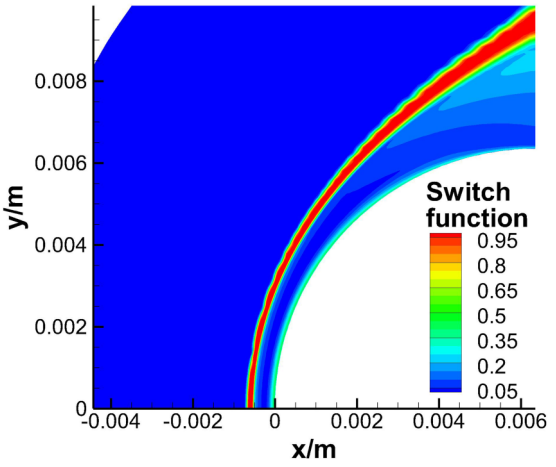

FIG. 17. Switch function contours of hypersonic air chemical nonequilibrium flow.

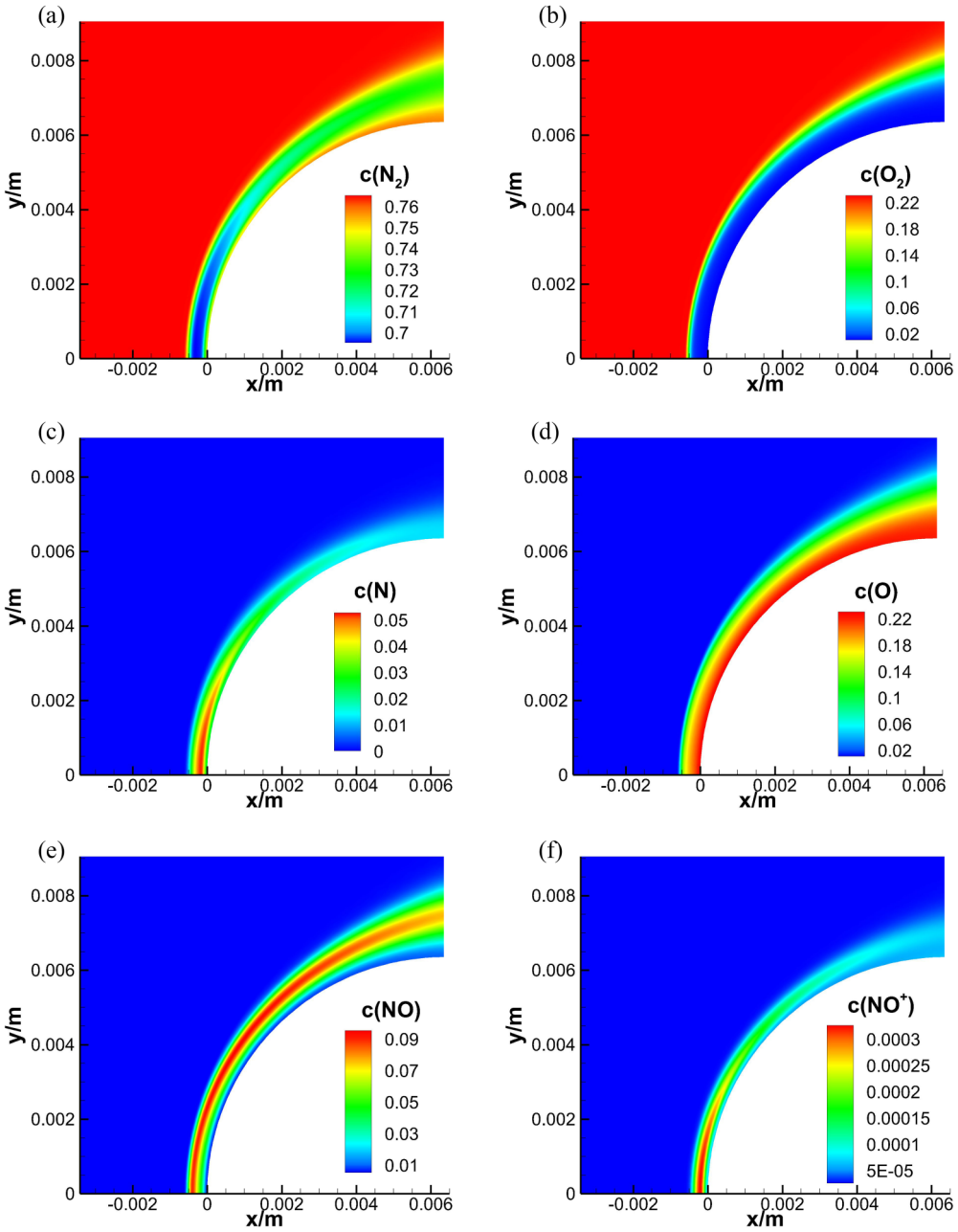

FIG. 18. Mass fraction contours of different species: (a) species N_2, (b) O_2, (c) N, (d) O, (e) NO, and (f) NO^+.

To validate whether the multicomponent LBFS has the "carbuncle" phenomenon in reacting flow under the condition of unfavorable grid aspect ratio [41], in this calculation, the aspect ratio of the grid is changed from 5 to 1 near the symmetric axis. Two typical upwind schemes, namely, the Roe scheme [42] with Harten's entropy correction [43] and the AUSM+ scheme, are selected for comparison. The temperature contours near the symmetric axis both in the presence and absence of chemical reaction conditions are shown in Fig. 12. When there is no chemical reaction, as shown in Figs. 12(a), 12(c), and 12(e), only the AUSM+ scheme shows a slight "carbuncle" phenomenon where the bow shock is distorted near the axisymmetric boundary. When chemical reactions are considered in the flow field, as shown in Figs. 12(b), 12(d), and 12(f), the "carbuncle" phenomenon occurs in both the Roe scheme and the AUSM+ scheme, while the multicomponent LBFS well captures the shock wave. Therefore, in this test case, the multicomponent LBFS is carbuncle-free whether the strong chemical reactions exist or not, even for the grid with unit aspect ratio. It is a great superiority compared with typical upwind schemes, which need a grid with a larger aspect ratio or additional numerical dissipation at the axisymmetric boundary [41].

B. Hypersonic air chemical nonequilibrium flow

To assess the performance of the multicomponent LBFS in highly nonequilibrium and very large temperature range

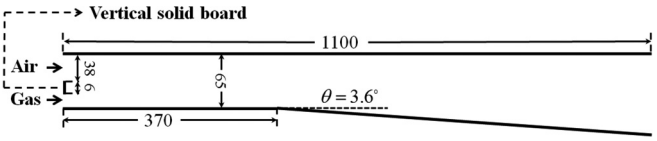

FIG. 19. Configuration of simplified dual combustion chamber (unit: mm).

conditions, hypersonic air chemical nonequilibrium flow over a sphere with a radius of 6.35 mm [44] is simulated in this section. The two-dimensional axisymmetric multicomponent N-S equations are solved on a structured grid with 100 × 100 cells, which is shown in Fig. 13, and the positive amplification factor $C = 15$ is used in this case. The air chemistry model is listed in Table V, which contains seven species (O_2, N_2, O, N, NO, NO^+, and e^-) and seven reactions [45]. The corresponding reaction coefficients and the thermodynamic properties of different species can be found in Ref. [45].

The free stream conditions are listed in Table VI. The wall boundary has a fixed temperature of 2000 K, and the noncatalytic wall condition is adopted. The nonreflecting condition is utilized for the far field, and the axisymmetric boundary condition is used along the line $y = 0$ m. The references of simulation parameters are listed in Table VII.

Figure 14 shows the comparison of the shock wave detachment distance obtained by the present solver and the experimental measurement [44], and Fig. 15 compares the calculated mass fraction of different species along the stagnation line with the calculation data from Ref. [46]. The results of multicomponent LBFS are in good agreement with the experimental and computational data. This shows that the multicomponent LBFS is suitable for the nonequilibrium flow with a large temperature range, and the chemical nonequilibrium effect can be well computed.

The temperature and switch function contours are shown in Figs. 16 and 17, respectively. Since the temperature behind the shock is above 9000 K, the air reacts violently downstream of the shock wave, and the region of switch function near 1.0 is thicker than the shock wave. Due to the fixed wall temperature and the combined reactions, the switch function has a small value near the wall. All these help the multicomponent LBFS to capture the strong bow shock and nonequilibrium reaction structure. It is worth noting that although the value of switch function in the boundary layer is not close to zero, in Figs. 14 and 15, the positions of shock waves and species distributions are in good agreement with the references. This shows that the switch function expressed by using temperature and pressure in Eq. (43) is appropriate for reacting flow in which the reacting zone may not be the same as the position of bow shock.

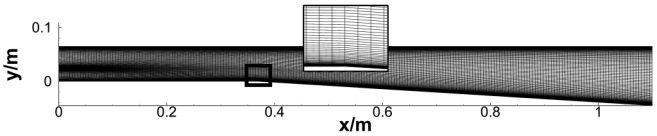

FIG. 20. Computational domain for supersonic combustion flow of ethylene.

TABLE VIII. Chemistry model [49].

No.	Reaction
1	$C_2H_4 + O_2 = 2CO + 2H_2$
2	$2CO + O_2 = 2CO_2$
3	$2H_2 + O_2 = 2H_2O$

The mass fraction contours of different species are shown in Fig. 18. The nitrogen is very hard to react, so a little of it decomposes downstream of the shock and quickly combines near the wall. Since the decomposition temperature of oxygen is relatively low, the oxygen is severely consumed after shock waves. Corresponding to the decomposition of nitrogen and oxygen, the mass fractions of nitrogen atoms and oxygen atoms are increased as the mass fractions of nitrogen and oxygen decrease. As the concentration of nitrogen atoms and oxygen atoms increases downstream of the shock wave, the formation of nitric oxide is fast at the initial stage and it becomes slow for the fall of temperature and the reduction of nitrogen atoms. Due to the chemical nonequilibrium effect, the high concentration area of nitric oxide ion is located slightly downstream at the high concentration region of nitric oxide.

C. Supersonic combustion flow of ethylene

The third case is chosen to examine the solver's ability for simulation of incomplete combustion flow with complex flow structure. In this case, a simplified dual combustion chamber [47] with supersonic combustion flow of ethylene is considered. The configuration of this chamber is illustrated in Fig. 19. The two-dimensional multicomponent N-S equations are solved on a structured grid with 130 × 220 cells, which is shown in Fig. 20, and the positive amplification factor C is set as 10 in this case. The entire flow field is considered to be fully turbulent, and a modified Spalart-Allmaras (S-A) one-equation turbulence model [48] is used.

The chemistry model listed in Table VIII, which contains seven species (C_2H_4, O_2, N_2, H_2, CO, H_2O, and CO_2) and three reactions [49], is used for simulation. The same as Sec. IV A, this case also uses the methods and database from CHEMKIN [38] to calculate the transport properties of each species and gas mixture. The free stream conditions are listed in Table IX. The adiabatic and noncatalytic condition is used for the wall, and the nonreflecting condition is utilized for the far field. It is noted that the vertical solid board is treated as a wall boundary in numerical simulation. For convenience, the references of simulation parameters are listed in Table X.

TABLE IX. Free stream conditions for supersonic combustion flow of ethylene.

				Mass fraction				
Flow	p (MPa)	T (K)	Ma	$c(C_2H_4)$	$c(O_2)$	$c(CO_2)$	$c(H_2O)$	$c(N_2)$
Air	0.0977	491.9	2.09	0.0	0.2330	0.0	0.0520	0.7150
Gas	0.1731	1771.9	1.25	0.1059	0.0103	0.1205	0.1566	0.6067

TABLE X. References of simulation parameters for supersonic combustion flow of ethylene.

Parameters	Boundary conditions	Chemical kinetics model	Thermodynamic database
Reference	[47]	[49]	[38]

Figure 21 shows the comparison of the pressure distribution on the chamber wall. It can be seen that the pressure profile of the multicomponent LBFS has only a little difference as compared with the AUSM+ scheme, and both of them match well with the numerical results from Ref. [47]. It is worth pointing out that the grid, chemical reaction model, space discrete scheme, and turbulence model in Ref. [47] are all less accurate as compared with this work.

As shown in Fig. 22(a), the high-temperature area is concentrated in the shear layer, where the air and gas are mixing to be the main reaction area. Notice that the temperature is especially high in the area where the shock wave passes through, and it plays a role of heating and mixing. In Fig. 22(b), the switch function contours clearly display the shock wave and reacting areas, which makes the computation stable.

The mass fractions of species CO and CO_2 are shown in Fig. 23. The maximum mass fraction of species CO_2 is about 0.1206, which is only a little higher than the mass fraction in the free stream. Only a little fuel completely reacts, and some of the species CO_2 is decomposed to species CO at high temperature. Due to the slow chemical reaction of the hydrocarbon fuel and the high flow velocity, the combustion in the chamber is weak and incomplete.

V. CONCLUSIONS

This paper develops a multicomponent LBFS for simulation the multicomponent compressible viscous reacting flows. The core of multicomponent LBFS is computing the inviscid flux by using the local solution of the one-dimensional lattice Boltzmann equation, while the viscous flux is evaluated using the traditional central difference method. Three key features of the present solver are listed as follows: (1) The total density at the cell interface is computed by the summation of the density distribution function, while the densities of different species are calculated by the mass fractions and density distribution functions from the left and right sides. This treatment maintains the advantage of the LBM in the density computation and gives the densities of different species by using the idea of streaming. (2) The enthalpy is used to represent the internal energy, and the temperature at the cell interface is estimated by Newton iteration. This feature considers the different physical properties of different species and provides a method for calculating the temperature. (3) The effects of reaction and grid aspect ratio are introduced to the switch function of the multicomponent LBFS. This improvement can reduce the high requirement of grid quality, and the numerical dissipation can be added properly near the unsmooth region such as the shock wave and combustion front. Moreover, since the developed multicomponent nonfree parameter D1Q4 model is applied only in the normal direction of the cell interface, a three-dimensional multicomponent LBFS can be easily obtained by using the coordinate transformation.

Several benchmark problems are used to validate the multicomponent LBFS. Numerical results show that the developed solver can provide satisfactory predictions for fluid flow problems under the condition of a large temperature range, complex chemical reaction model, fast- and slow-reacting flow field, complex geometry, and flow field structure. Moreover, the computed distributions of flow variables and species mass fractions are in good agreement with those of the AUSM+ scheme and experimental/computational results shown in the

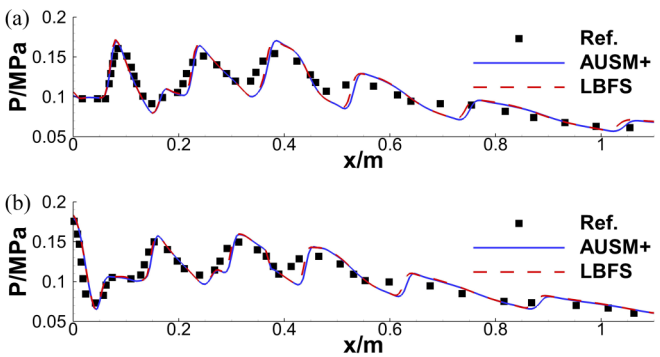

FIG. 21. Comparison of the pressure distribution on the chamber wall: (a) upper surface and (b) lower surface.

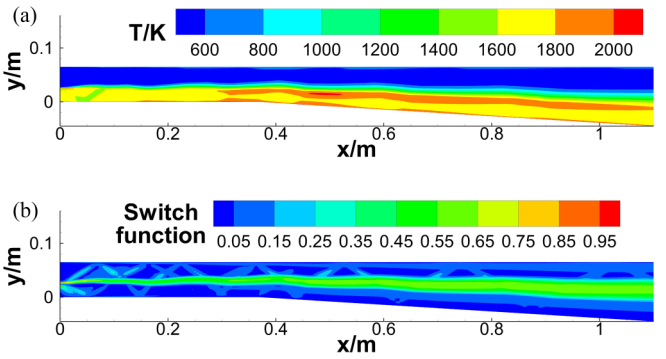

FIG. 22. Temperature and switch function contours of the chamber: (a) temperature contours and (b) switch function contours.

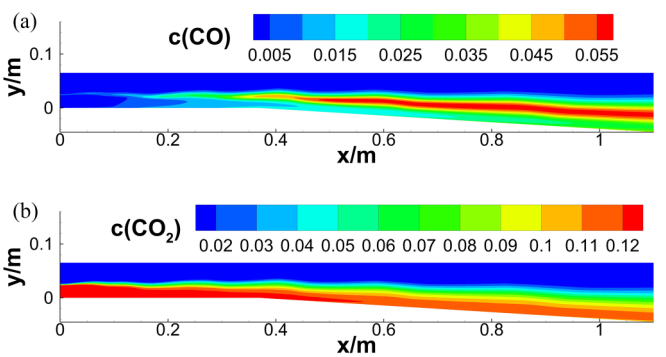

FIG. 23. Mass fraction contours of species CO and CO_2: (a) species CO and (b) species CO_2.

references. In the test case, the multicomponent LBFS demonstrates good convergence properties, and it is also shown to be carbuncle-free, even for the unfavorable aspect ratio grid. It is believed that the developed multicomponent LBFS has a great potential for solving complicated reacting flows.

ACKNOWLEDGMENTS

This work was supported by the China Scholarship Council (Grant No. 201806830086) and the Postgraduate Research & Practice Innovation Program of Jiangsu Province (Grant No. KYCX18_0247).

[1] R. R. Nourgaliev, T. N. Dinh, T. G. Theofanous, and D. Joseph, The lattice Boltzmann equation method: Theoretical interpretation, numerics and implications, Int. J. Multiphase Flow **29**, 117 (2003).

[2] S. Succi, *The Lattice Boltzmann Equation: For Fluid Dynamics and Beyond* (Oxford University, New York, 2001).

[3] Y. Wang, C. Shu, H. B. Huang, and C. J. Teo, Multiphase lattice Boltzmann flux solver for incompressible multiphase flows with large density ratio, J. Comput. Phys. **280**, 404 (2015).

[4] Z. L. Guo and T. S. Zhao, Lattice Boltzmann model for incompressible flows through porous media, Phys. Rev. E **66**, 036304 (2002).

[5] A. J. C. Ladd and R. Verberg, Lattice-Boltzmann simulations of particle-fluid suspensions, J. Stat. Phys. **104**, 1191 (2001).

[6] S. Z. Chen, K. Xu, C. B. Lee, and Q. D. Cai, A unified gas kinetic scheme with moving mesh and velocity space adaptation, J. Comput. Phys. **231**, 6643 (2012).

[7] S. Succi, G. Bella, and F. Papetti, Lattice kinetic theory for numerical combustion, J. Sci. Comput. **12**, 395 (1997).

[8] K. Yamamoto, X. Y. He, and G. D. Doolen, Simulation of combustion field with lattice Boltzmann method, J. Stat. Phys. **107**, 367 (2002).

[9] O. Filippova and D. Hanel, A novel lattice BGK approach for low Mach number combustion, J. Comput. Phys. **158**, 139 (2000).

[10] B. Yan, A. G. Xu, G. C. Zhang, Y. J. Ying, and H. Li, Lattice Boltzmann model for combustion and detonation, Front. Phys. **8**, 1 (2013).

[11] F. J. Alexander, H. Chen, S. Chen, and G. D. Doolen, Lattice Boltzmann model for compressible fluids, Phys. Rev. A **46**, 1967 (1992).

[12] K. Qu, C. Shu, and Y. T. Chew, Alternative method to construct equilibrium distribution functions in lattice-Boltzmann method simulation of inviscid compressible flows at high Mach number, Phys. Rev. E **75**, 036706 (2007).

[13] L. M. Yang, C. Shu, and J. Wu, A moment conservation-based non-free parameter compressible lattice Boltzmann model and its application for flux evaluation at cell interface, Comput. Fluids **79**, 190 (2013).

[14] S. Geller, M. Krafczyk, J. Tölke, S. Turek, and J. Hron, Benchmark computations based on lattice-Boltzmann, finite element and finite volume methods for laminar flows, Comput. Fluids **35**, 888 (2006).

[15] K. Qu, C. Shu, and Y. T. Chew, Simulation of shock-wave propagation with finite volume lattice Boltzmann method, Int. J. Mod. Phys. C **18**, 447 (2007).

[16] Q. Li, Y. L. He, Y. Wang, and W. Q. Tao, Coupled double-distribution-function lattice Boltzmann method for the compressible Navier-Stokes equations, Phys. Rev. E **76**, 056705 (2007).

[17] S. Ubertini and S. Succi, Recent advances of lattice Boltzmann techniques on unstructured grids, Prog. Comput. Fluid Dyn. **5**, 85 (2005).

[18] N. Rossi, S. Ubertini, G. Bella, and S. Succi, Unstructured lattice Boltzmann method in three dimensions, Int. J. Numer. Methods Fluids **49**, 619 (2005).

[19] T. Krüger, H. Kusumaatmaja, A. Kuzmin, O. Shardt, G. Silva, and E. M. Viggen, *The Lattice Boltzmann Method, Principles and Practice* (Springer, Switzerland, 2017).

[20] C. Z. Ji, C. Shu, and N. Zhao, A lattice Boltzmann method-based flux solver and its application to solve shock tube problem, Mod. Phys. Lett. B **23**, 313 (2009).

[21] L. M. Yang, C. Shu, W. M. Yang, and Y. Wang, Extension of lattice Boltzmann flux solver for simulation of compressible multi-component flows, Mod. Phys. Lett. B **32**, 1840001 (2018).

[22] L. M. Yang, C. Shu, and J. Wu, Extension of lattice Boltzmann flux solver for simulation of 3D viscous compressible flows, Comput. Math. Appl. **71**, 10 (2016).

[23] L. M. Yang, C. Shu, and J. Wu, A hybrid lattice Boltzmann flux solver for simulation of viscous compressible flows, Adv. Appl. Math. Mech. **8**, 887 (2016).

[24] D. Zhou, Z. L. Lu, and T. Q. Guo, A rotating reference frame-based lattice Boltzmann flux solver for simulation of turbomachinery flows: A rotating frame-based LBFS for simulation of turbomachinery flows, Int. J. Numer. Methods Fluids **83**, 561 (2017).

[25] Y. Li, H. Z. Yuan, X. D. Niu, Y. Y. Yang, and S. Shu, WENO scheme-based lattice Boltzmann flux solver for simulation of compressible flows, Commun. Comput. Phys. **23**, 1012 (2018).

[26] M. S. Liou, Progress towards an improved CFD method - AUSM+, in *Proceedings of the 12th Computational Fluid Dynamics Conference, San Diego, CA* (AIAA, 1995), p. 606.

[27] J. F. Wang, Y. Z. Wu, W. D. Ji, X. F. Fan, F. M. Zhao, and Z. J. Lyu, Progress in numerical simulation techniques of hypersonic aerodynamic problems, Acta Aeronaut. Astronaut. Sin. **36**, 159 (2015).

[28] J. Blazek, *Computational Fluid Dynamics, Principles, and Applications* (Butterworth-Heinemann, Oxford, 2015).

[29] S. W. Ouyang and Z. Q. Xie, *High Temperature Nonequilibrium Air Flow* (National Defense Industry, Beijing, 2001).

[30] C. K. Law, *Combustion Physics* (Cambridge University, New York, 2006).

[31] Q. H. Yu, Numerical simulation for 3-D hypersonic flows on hybrid meshes and parallelization, Master's thesis, Nanjing University of Aeronautics and Astronautics, 2006.

[32] M. Pandolfi and D. D'Ambrosio, Numerical instabilities in upwind methods: Analysis and cures for the "carbuncle" phenomenon, J. Comput. Phys. **166**, 271 (2001).

[33] A. Jameson, W. Schmidt, and E. Turkel, Numerical solutions of the Euler equations by finite volume methods using Runge-Kutta time-stepping schemes, in *Proceedings of the 14th Fluid and Plasma Dynamics Conference, Palo Alto, CA* (AIAA, 1981).

[34] T. J. Barth and D. C. Jespersen, The design and application of upwind schemes on unstructured meshes, in *Proceedings of the 27th Aerospace Sciences Meeting, Reno, NV* (AIAA, 1989).

[35] V. Venkatakrishnan, Convergence to steady-state solutions of the Euler equations on unstructured grids with limiters, J. Comput. Phys. **118**, 120 (1995).

[36] H. F. Lehr, Experiments on shock-induced combustion, Astronaut. Acta **17**, 589 (1972).

[37] G. A. Moretti, A new technique for the numerical analysis of nonequilibrium flows, AIAA J. **3**, 223 (1965).

[38] R. J. Kee, F. M. Rupley, and E. Meeks, CHEMKIN-III: A FORTRAN chemical kinetics package for the analysis of gas-phase chemical and plasma kinetics, Sandia National Laboratories Rep. No. SAND–96-8216, 1996.

[39] M. Soetrisno and S. T. Imlay, Simulation of the flow field of a ram accelerator, in *Proceedings of the 27th Joint Propulsion Conference, Sacramento, CA* (AIAA, 1991).

[40] Y. B. Zeldovich, On the theory of the propagation of detonation in gaseous systems, NASA Tech. Rep. No. NACA TM-1261, 1950.

[41] R. W. MacCormack, The carbuncle CFD problem, in *Proceedings of the 49th AIAA Aerospace Sciences Meeting including the New Horizons Forum and Aerospace Exposition, Orlando, Florida* (AIAA, 2011).

[42] P. L. Roe, Approximate Riemann solvers, parameter vectors, and difference schemes, J. Comput. Phys. **43**, 357 (1981).

[43] A. Harten and J. M. Hyman, Self-adjusting grid methods for one-dimensional hyperbolic conservation laws, J. Comput. Phys. **50**, 235 (1983).

[44] R. K. Lobb, Experimental measurement of shock detachment distance on spheres fired in air at hypervelocities, AGARDograph **68**, 519 (1964).

[45] R. N. Gupta, J. M. Yos, and R. A. Thompson, A review of reaction rates and thermodynamic and transport properties for the 11-species air model for chemical and thermal nonequilibrium calculations to 30000 K, NASA Tech. Rep. No. NASA-TM-101528, 1989.

[46] H. Y. Li, Numerical Simulation of hypersonic and high temperature gas flow fields, Ph.D. thesis, China Aerodynamics Research and Development Center, 2007.

[47] C. Wang, M. Situ, J. H. Ma, and M. L. Yang, Numerical simulation on supersonic combustion of fuel-rich hot gas, J. Propul. Technol. **21**, 60 (2000).

[48] J. Dacles-Mariani, G. G. Zilliac, J. S. Chow, and P. Bradshaw, Numerical/experimental study of a wingtip vortex in the near field, AIAA J. **33**, 1561 (1995).

[49] R. A. Baurle, T. Mathur, M. R. Gruber, and K. R. Jackson, A numerical and experimental investigation of a scramjet combustor for hypersonic missile applications, in *Proceedings of the 34th AIAA/ASME/SAE/ASEE Joint Propulsion Conference and Exhibit, Cleveland, OH* (AIAA, 1998).